MULTI-OBJECTIVE OPTIMIZATION OF SATELLITE DEORBITING MANEUVERS CONSIDERING COLLISION RISK

Livia MARCIANO[(1)], Giuseppe DI PASQUALE[(2)], and Manuel SANJURJO RIVO[(3)]

[(1)] *Universidad Carlos III de Madrid, Av. de la Universidad, 30 (Spain), lmarcian@pa.uc3m.es*
[(2)] *IENAI SPACE, Av. Gregorio Peces Barba, 1 (Spain), giuseppe.dipasquale@ienai.space*
[(3)] *Universidad Carlos III de Madrid, Av. de la Universidad, 30 (Spain), msanjurj@ing.uc3m.es*

ABSTRACT

The accumulation of space objects in Low Earth Orbit (LEO) from decades of unregulated activities and recent mega-constellations has heightened collision risks among active satellites and debris. Effective disposal is critical and can be performed via on-board propulsion—either electric or chemical—with the optimal strategy balancing maneuvering effort against collision probability based on orbit and residence time. This work presents a multi-objective approach to automating the search for optimal deorbiting maneuvers that minimize propulsive effort and collision probability. The method utilizes a non-singular orbital elements formulation, accounting for Earth's oblateness and atmospheric drag, as modeled by the NRLMSISE-00, whose parameter uncertainties are analyzed in the results. The approach extends the capabilities of the DRAMA's ARES tool, enabling collision probability computation throughout the deorbiting process via trajectory discretization. The resulting Pareto front provides mission designers with a range of optimal solutions and highlights how different propulsion technologies and varying solar activity impact disposal strategies, ultimately contributing to the long-term sustainability of LEO operations.

Keywords: space debris; deorbiting; collision probability; multi-objective optimization.

1. INTRODUCTION

The accumulation of space debris in Low Earth Orbit (LEO) increasingly threatens satellite operations and long-term space sustainability. This problem is worsened by the increasing number of satellites launched and the rise of mega-constellations. Consequently, the probability of collisions rises, which increases the risk of collisions and can result in satellite fragmentation and the generation of additional debris, as seen in events such as the 1996 Cerise-Ariane incident, the 2007 Chinese anti-satellite test, and the 2009 Iridium-Cosmos collision [21]. The most extreme outcome is captured by the Kessler Syndrome, which suggests that collisions could eventually trigger a chain reaction, making LEO entirely uninhabitable for human activities.

Addressing these challenges requires the implementation of effective debris mitigation strategies, such as Post-Mission Disposal (PMD) and Active Debris Removal (ADR). These two fundamental approaches are crucial for reducing the growing volume of space debris and ensuring the long-term sustainability of space operations. The European Space Agency's Zero Debris [11] approach underlines the need for optimized deorbiting maneuvers.

A critical concern throughout these strategies is the collision risk, which affects both operational and decommissioning phases. Reducing collision probability is essential for ensuring mission safety and the long-term sustainability of space activities.

Several methodologies are used to estimate collision probability in the context of space debris and celestial mechanics. They are connected through their approach to modeling the likelihood of space object collisions, but they differ in their assumptions, mathematical formulations, and computational implementations. Some examples include LUCA2 [19], the CUBE algorithm [5], and Öpik's theory [26, 24]. However, in the context of this work, the ARES [9] module—part of ESA's DRAMA tool [10]—is used to accurately compute collision risks during the deorbiting phase.

The literature highlights a range of strategies for deorbiting that aim to reduce both fuel consumption and collision risks in LEO. Chen *et al.* [2] propose a three-stage active debris removal method where a primary spacecraft deploys multiple small, electrically propelled satellites. These satellites push debris into lower orbits using genetic algorithms and two-impulse rendezvous techniques, optimizing the mission sequence under constraints such as fuel, time, and available spacecraft. While effective, this approach may benefit from a deeper analysis of perturbative forces.

Verri *et al.* [22] focus on optimizing low-thrust, many-revolution transfers by employing a modified version of Edelbaum's theory that accounts for the J_2 effects. Their work targets either minimum deorbit time or reduced propellant consumption, emphasizing the importance of optimal thrust switching strategies in achieving efficient deorbiting.

Proc. 9th European Conference on Space Debris, Bonn, Germany, 1–4 April 2025, published by the ESA Space Debris Office
Editors: S. Lemmens, T. Flohrer & F. Schmitz, (http://conference.sdo.esoc.esa.int, April 2025)

Gaglio *et al.* [14] introduce a drag-based deorbiting method that leverages changes in a spacecraft's aerodynamic profile to enhance atmospheric drag. Using MATLAB's GPOPS-II and an hp-adaptive Gaussian quadrature orthogonal collocation method, they derive time-optimal decay trajectories under an exponential atmospheric model. This strategy, while precise for circular orbits, could be further improved by incorporating real-time control methods and more realistic process models.

Complementing these active approaches, Colombo et al. [3] and Fukii *et al.* [13] investigate passive deorbiting techniques. Colombo et al. compare solar sails and balloons by balancing re-entry time against cumulative collision probabilities, whereas Fukii *et al.* assess the use of low-thrust laser-ablation methods to maintain collision risks within safe limits. Finally, Radtke *et al.* [18] integrate active and passive deorbiting measures in mega-constellation operations to mitigate long-term debris risks, ensuring sustainable use of increasingly congested orbital environments.

As highlighted in the literature review, previous studies on decay optimization primarily focus on traditional objectives such as propellant consumption or decay duration. In contrast, this work introduces the incorporation of collision risk into a multi-objective optimization process.

Furthermore, this work proposes a methodology to improve the estimation of collision probability during the decay phase, thereby enhancing the reliability and accuracy of the results.

The analyses presented focus on low-thrust propulsion systems, which have gained prominence in recent years, though the methodology can also be applied to other reentry technologies.

The content of this article is structured as follows: Section 2 introduces the problem along with the necessary mathematical foundations, followed by Section 3, which provides a detailed description of the proposed methodology. Section 4 then presents numerical applications of the methodology, while Section 5 summarizes the key findings and conclusions.

2. PROBLEM STATEMENT

The decommissioning phase of a satellite is a critical aspect of mission design, requiring passivation of hazardous equipment and removal from congested orbital regions. In LEO, this translates into deorbiting maneuvers, whose design requires careful balance of multiple factors, including the duration, the amount of resources expended, and the risk of collision with other bodies.

This problem can be treated as a multi-objective optimization problem, which is presented alongside its key components in the following subsections.

2.1. Optimization Problem

The optimization problem, whose results are shown in the following chapter, is a control problem in which the goal is to minimize a set of objectives while ensuring compliance with system dynamics and constraints.

Mathematically, the problem is formulated as follows:

$$\begin{array}{rl} min_{\boldsymbol{u}\in U} & \boldsymbol{J}(t,\boldsymbol{y}(t)), \\ \textit{subject to} & \dot{\boldsymbol{y}}(t) = \boldsymbol{f_d}(t,\boldsymbol{y}(t),\boldsymbol{u}(t)) \\ & \boldsymbol{y}(t_0) - \boldsymbol{\psi}_0 = 0, \\ & \boldsymbol{y}(t_f) - \boldsymbol{\psi}_f = 0, \end{array} \tag{1}$$

where $\boldsymbol{y}$ represents the state of the dynamical system, and $\boldsymbol{u}$ the controls, which are the design variables. The objective vector $\boldsymbol{J}$ contains the objectives to be minimized, which could include a combination of ΔV, propellant mass (m_p), decay duration (t_f) and the probability of collision throughout the decay (p_c).

The states are subject to dynamics, represented by the function $\boldsymbol{f_d}$, and a set of boundary conditions, expressed by the vectors $\boldsymbol{\psi_0}$ and $\boldsymbol{\psi_f}$, for the initial and final conditions respectively.

2.2. Deorbiting dynamics

The dynamics of the decay phase in Eq. (1) is described by the following differential equations system:

$$\dot{\boldsymbol{y}}(t) = \boldsymbol{f_d} = A(\boldsymbol{y}(t))\boldsymbol{u}(t) + \boldsymbol{b}(\boldsymbol{y}(t)), \tag{2}$$

where the matrix A and vector $\boldsymbol{b}$ are defined as in [4], representing Gauss variational equations. The state vector contains the Modified Equinoctial Elements (MEE), namely p, f, g, h, k, and L, and the satellite mass (m):

$$\boldsymbol{y} = [p, f, g, h, k, L, m]^T. \tag{3}$$

It is possible to transform the MEE formulation into Classical Orbital Elements (COE), via the transformation (ϕ) [25]:

$$\boldsymbol{y}_{coe} = \phi\left(\boldsymbol{y}_{mee}\right), \tag{4}$$

where $\boldsymbol{y}_{mee} \subset \boldsymbol{y}$. It is possible to apply the inverse transformation ϕ^{-1} to retrieve MEE from COE. This allows to specify the boundary conditions for the problem in an easy manner. In particular, $\boldsymbol{\psi}_0$ contains the orbital elements and the initial mass. On the other hand, the only element fixed in the final conditions is the final semi-major axis (a_f), whereas the other components are left free. Therefore, $\boldsymbol{\psi}_f = [a(t_f) - a_f]$.

The perturbations considered in Eq. (2) include Earth's oblateness effects (specifically the J_2 harmonic), modeled using the formulation from [4], and atmospheric drag, computed with the NRLMSISE-00 density model [17].

2.3. Guidance policy

The optimization problem outlined in Eq. (1) requires finding the time-dependent controls, $\boldsymbol{u}$, which are bounded within a set U and minimize a given set of objectives. In this work, the following guidance policy is adopted:

$$\alpha^* = \pi + arctan\left(\frac{e\sin(\theta)}{1 + e\cos(\theta)}\right), \quad \beta^* = 0, \qquad (5)$$

in which α^* is the optimal in-plane angle, β^* the optimal out-of-plane angle, e the orbit eccentricity and θ the current true anomaly.

This policy fundamentally states that to decrease the semi-major axis, it is best to direct the thrust in plane and opposite to the velocity vector [6]. This represents near-optimal guidance for minimum-energy solutions variations of semi-major axis, under the assumption of circular orbits, a condition generally satisfied in low-thrust trajectories.

Due to the adoption of this guidance and the constraints imposed, the firing time, called t_{thr}, is the only remaining design variable of the problem.

The evaluation of the objectives from Eq. (1) can be carried out via numerical integration and post-processing of the results obtained. The propellant mass (m_p):

$$m_p = m(t_0) - m(t_f), \qquad (6)$$

whereas the ΔV—which is fundamentally equivalent to m_p— can be obtained applying Tsiolkovsky, and the decay time (t_f) is the time at which the terminal conditions are met (the re-entry boundary is reached).

2.4. Collision probability

The computation of probability of collision (P) between two objects can be found integrating the normalized Gaussian probability density for the position covariance ($f(x, y, z)$):

$$P = \iiint_V f(x, y, z)dx\, dy\, dz, \qquad (7)$$

in which the objects are usually assumed to be spheres [16]. This equation provides a general tool to compute the probability of collision between two objects, which is critical for the estimation of collision events.

However, for design purposes, due to the large amount of debris, and the unknown location and objects encountered throughout the mission, a flux approach is preferred. A flux approach approximates populations of debris and their evolution over time, which is a function of the launches, satellite operations, and the decay of debris and satellites. MASTER [8] represents one of these spatial and temporal models, providing the flux for different debris sizes.

Ultimately, the cumulative probability of collision (p_c) is computed using the trajectory history, thus the states over time $\boldsymbol{y}(t)$, obtained as the integral over time of the instantaneous probability:

$$p_c = \int_{t_0}^{t_f} P(t, \boldsymbol{y})\, dt. \qquad (8)$$

3. METHODOLOGY

The methodology used to solve the optimization problem outlined in the previous section is illustrated in Figure 1 using the Design Structure Matrix (DSM) standard. The schematic represents the key inputs, outputs, and process blocks in a sequential framework, each of which is described below.

The process begins with the optimizer (a line search in this case, though alternative gradient-based or heuristic methods can be used), which selects a firing time (t_{thr}) (Step 1). Parameters such as the drag area (A_d), thruster properties (T, I_{sp}) are inputs at this stage. The system then numerically propagates Eq. (2) using the guidance policy from Eq. (5) (Step 2).

The propagation step produces the state trajectory ($\boldsymbol{y}^*(t)$), propellant mass (m_p), and decay time (t_f), starting from the initial state $\boldsymbol{y}(t_0)$. These outputs are then passed to the discretizer (Step 3), which generates a discretized trajectory of n intervals ($\boldsymbol{t}_d$ and $\boldsymbol{y}_d$).

Finally, ESA's software tool Assessment of Risk Event Statistics (ARES) is executed (Step 4), provided of the collision area (A_c), which represents the size of the object, and the maximum and minimum particle size ($\boldsymbol{p}_s$) computing the cumulative collision probability (p_c) according to the procedure detailed in the following section.

The optimizer iterates over the steps described, ultimately generating the set of optimal objectives (m_p^*, t_f^*, p_c^*), which typically results in a multi-dimensional Pareto front.

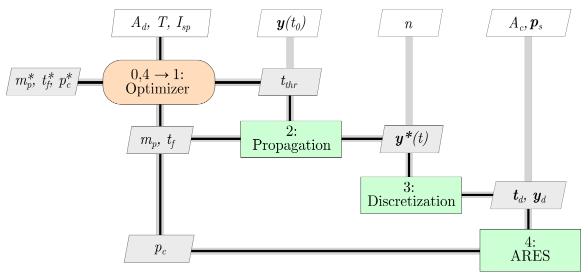

Figure 1: Design structure matrix of the methodology.

3.1. Enhanced collision probability computation

A key contribution of this work is an enhanced method for computing collision probability along the deorbiting trajectory. This method corresponds to Steps 3 and 4 in Figure 1, where the trajectory is discretized and the collision probability is computed using ARES, providing an estimate over a varying orbit.

To understand the rationale behind this approach, it is essential to review some key aspects of ARES.

3.1.1. Background: ARES collision probability model

ESA's Debris Risk Assessment and Mitigation Analysis (DRAMA) software evaluates space missions' compliance with international space debris mitigation requirements. Within DRAMA, the ARES module computes the Annual Collision Probability (ACP) by assessing collision risks based on averaged orbital elements and debris flux data from MASTER [8].

ARES relies on a set of key assumptions:

- *Spacecraft shape*: is assumed to be spherical, with a radius R_{sc}.
- *Reference orbit*: is described using averaged elements, excluding the true anomaly since the model is not dependent on the location within the orbit.

Thus, the ACP is computed as:

$$\text{ACP} = \sum_{j=1}^{m} F_j \cdot \pi \cdot (R_{sc} + r_j)^2 , \tag{9}$$

where F_j represents the annual debris flux provided by MASTER [8], for the j-th population group, R_{sc} is the spacecraft radius (associated to its spherical cross-sectional area [15]), and r_j is the size of the corresponding debris element.

Additionally, ARES requires values for the minimum and maximum debris particle sizes (indicated by the vector $\boldsymbol{p}_s$, and the initial epoch.

An important observation is that ARES computes the annual collision probability for a nominal orbit, fundamentally assuming that this orbit is maintained (for example via station-keeping), hence does not cover evolving orbits, such as in the case of a decaying or deorbiting satellite.

3.1.2. Probability of collision throughout decay

Building onto the concepts and observations from the previous subsection, this work proposes an improved and efficient methodology for computing the cumulative collision probability along the deorbiting trajectory using ARES.

The instantaneous collision probability P can vary significantly for a satellite whose trajectory is evolving over time, such as a deorbiting satellite.

Given the high computational cost of ARES runs, a trajectory discretization strategy is adopted to reduce the number of calls, and a schematic is presented in Figure 2.

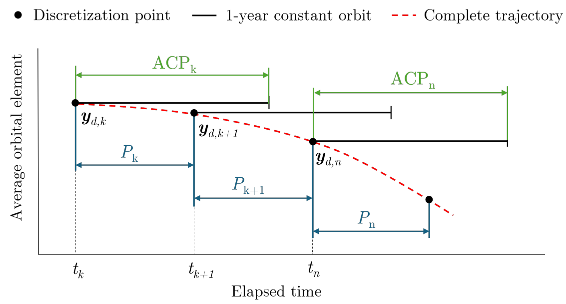

Figure 2: Schematic of discretization.

The procedure developed follows these key steps:

1. *Trajectory discretization*: the output trajectory ($\boldsymbol{y}^*$) is discretized in n intervals, using either a time or a semi-major axis (SMA) discretization. Based on each discretization point, the remaining parameters are interpolated into $\boldsymbol{y}_d$.

2. *ACP computation*: for each interpolated orbit, the ACP is computed with ARES. This assumes a 1-year constant orbit, as shown in Figure 2. Calling the ARES computation function χ_a (Eq. (9)):

$$\text{ACP}_k = \chi_a(t_k, \boldsymbol{y}_{d,k}) \quad \forall k \in [1, n], \tag{10}$$

where t_k is the time spent in the k-th interval, a component of the discretized time vector $\boldsymbol{t}_d$, and $\boldsymbol{y}_{d,k}$ is the k-th component of the discretized trajectory $\boldsymbol{y}_d$.

3. *Interval collision probability computation*: the collision probability within an interval (P_k) is computed as the ACP normalized by the time spent in each interval:

$$P_k = \frac{\text{ACP}_k \cdot t_k}{365 \cdot 24 \cdot 3600} \quad \forall k \in [1, n]. \tag{11}$$

4. *Probability of collision through the decay*: by summing all the P_k, it is possible to obtain the collision probability throughout the decay trajectory:

$$p_c = \sum_{k=1}^{n} P_k, \tag{12}$$

where n is the number of discrete trajectory intervals.

Table 1: Simulation parameters.

Parameter	Value	Unit
$F10.7_a$	150	-
$F10.7$	150	-
A_p	4	-
Minimum particle size	0.01	m
Maximum particle size	100	m
Drag coefficient	2.2	-
Reference area	0.06	m^2
Mass	10.0	kg
Epoch year	2000	-

3.2. Analysis of the discretization intervals

By observing the methodology presented in the previous subsection, we note that for sufficiently small intervals:

$$\lim_{n \to \infty} P_k = P, \tag{13}$$

hence, Eq. (12) would converge to Eq. (8).

While a higher n improves accuracy, it also increases computational cost. The proposed method balances efficiency and accuracy, enabling automated collision probability computation along deorbiting trajectories.

This section analyzes discretization intervals to determine the minimum n needed for accurate results with reduced computational effort. Two discretization strategies are compared: time-based and semi-major axis (SMA)-based.

The analysis considers a satellite deorbiting from two Sun-Synchronous Orbits (SSO) with different initial altitudes. The simulation parameters, listed in Table 1, assume a simplified case where the drag area (A_d) and collision cross-sectional area (A_c) are equal.

The first case examines an SSO orbit at 350 km altitude, with initial COEs given by :

$$\boldsymbol{y_0} = \begin{bmatrix} 6721.0 \text{ km} \\ 0.001 \\ 96.83° \\ 250.36° \\ 120.0° \\ 0.0° \end{bmatrix}. \tag{14}$$

For this orbit, computations were repeated for different values of n. Figure 3 illustrates the discretization for $n = 4$ and $n = 30$ based on the satellite's semi-major axis. Increasing n improves the trajectory approximation, while fewer intervals assume COEs remain constant over longer periods.

However, this comes at the cost of higher computational time, as more intervals increase the number of inputs to ARES.

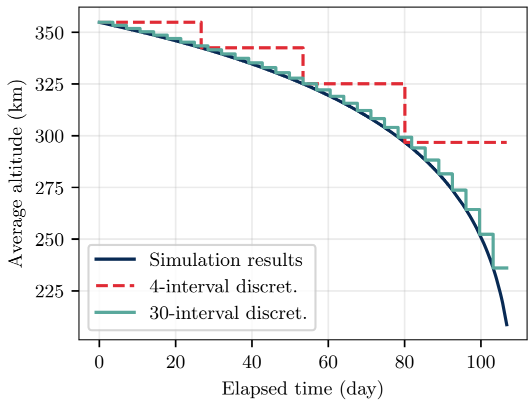

Figure 3: Time discretization example for an initial average with 4 and 30 intervals.

Figure 4 shows the relative error compared to the $n = 200$ case for both time-based and semi-major axis-based discretizations. This plot helps identify the point at which the error stabilizes. Notably, for $n \geq 40$, the relative error remains below 5%, with only minor residual oscillations.

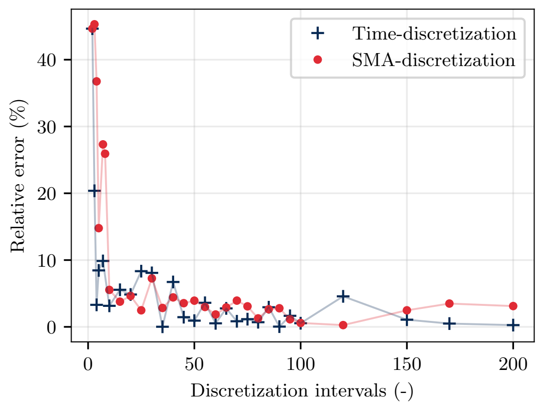

Figure 4: Relative error versus discretization intervals for time and semi-major axis-discretization in the case of an SSO at 350 km.

To better understand this oscillating behavior, Figure 5 presents the annual collision probability for different discretizations n. With more intervals, the probability oscillates significantly, likely due to discretization effects within MASTER's internal flux models. Conversely, fewer intervals introduce an averaging effect, smoothing out fluctuations. Thus, a sufficient number of intervals is essential to preserve the probability trend. Ultimately, this result confirms the observed behavior of p_c.

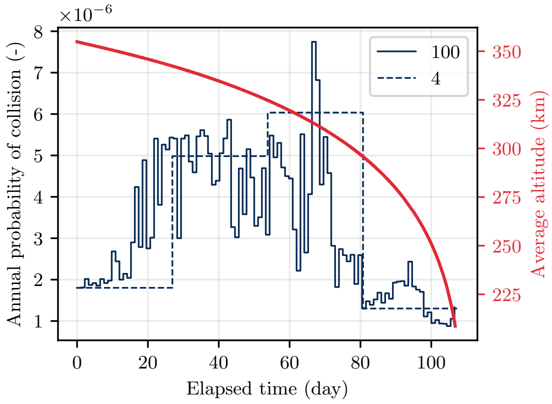

Figure 5: Annual collision probability and average altitude for $n = 4$ and $n = 100$.

The second case examines an SSO orbit at 520 km altitude, with initial COEs given by $\boldsymbol{y_0} = [6891.0\text{km}, 0.001, 96.45°, 250.36°, 120.0°, 0.0°]$.

Figure 6 shows a similar trend to Figure 4, but the higher altitude case exhibits more erratic behavior for the SMA-based discretization. This likely occurs because, with SMA discretization, more points are concentrated in the final part of the decay trajectory, where altitude changes more rapidly. In contrast, the time-based discretization distributes points more uniformly along the entire trajectory.

For the time-based discretization, $n = 40$ appears to be an appropriate minimum number of intervals.

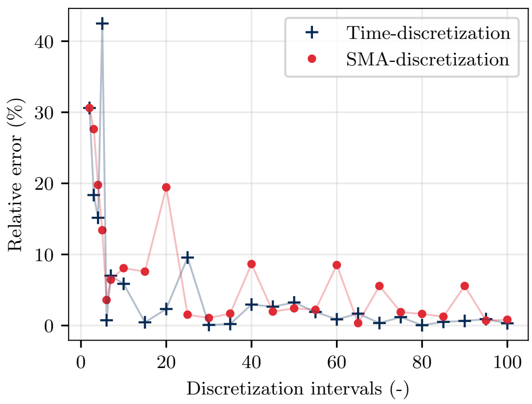

Figure 6: Relative error versus discretization intervals for time and semi-major axis-discretization in the case of an SSO at 520 km.

This analysis demonstrates that time-based discretization converges more rapidly and exhibits greater stability in deorbiting scenarios when evaluating collision probability along the decay trajectory. Consequently, the time-based approach is adopted in the numerical examples presented in Section 4.

Moreover, comparison with a single ARES run highlights the critical role of using a sufficiently high number of intervals, as it significantly refines the collision probability estimation. With $n = 40$ intervals in both cases, the estimate improves by up to 40%.

Table 2: Nanosatellite properties.

Parameter	Value	Unit
Top-facing area (A_1)	0.23	m^2
Lateral-facing area (A_2)	0.30	m^2
Frontal area (A_3)	2.1	m^2
Tumbling area (A_t)	0.877	m^2
Initial mass (m_0)	75.0	kg
Drag coefficient (C_D)	2.2	-

4. RESULTS AND ANALYSIS

This section presents numerical examples evaluating the effects of atmospheric drag uncertainty and propulsion system selection.

4.1. Simulation settings

The study considers an SSO at 520 km altitude, a densely populated region of LEO. The number of intervals is set to $n = 40$, as discussed in the previous chapter. To ensure realistic results, satellite properties are based on a commercial nanosatellite platform [1]. The satellite's geometric configuration is illustrated in Figure 7, with detailed properties listed in Table 2.

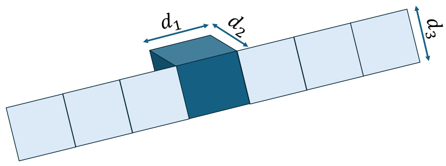

Figure 7: Schematic of the selected satellite (d_1 = d_2 = 480 mm; d_3 = 620 mm).

The frontal area is used for the cross-sectional area required in the collision probability computation (A_c), while the drag area (A_d) is assumed to correspond to the tumbling area, computed as:

$$A_t = \frac{1}{3}(A_1 + A_2 + A_3) \quad (15)$$

The propulsion systems' performance considered are based on commercial systems, including a Hall Effect

Table 3: Propulsion systems properties.

System	HET	FEEP	ATHENA
Thrust (mN)	2.5	0.84	1.75
Specific impulse (s)	850.0	3200.0	1500.0
Power (W)	60.0	80.0	60.0
Propellant mass (g)	600	440	700

Thruster (HET) [12], a Field Emission Electric Propulsion (FEEP) [7] and ATHENA (electrospray) [23]. Their properties are listed in Table 3.

4.2. Collision probability as objective

The first result presented is the generation of Pareto optimal front using collision probability as an objective.

The propulsion system firing time (t_{thr}) is the variable in Eq. (1). A firing time of $t_{thr} = 0.0$ corresponds to a natural decay trajectory, driven solely by atmospheric drag. For a given thrust-to-mass ratio, there exists a maximum value of t_{thr} that results in a *direct re-entry* trajectory.

As an example, Figure 8 illustrates the evolution of the average semi-major axis over time for two different firing times (30 and 45 days). The initial trajectory leg is identical for both cases. However, at $t = 30$ days, one of the trajectories enters a drag-only decay phase. This case requires less propellant (lower ΔV), but the decay time extends to nearly 80 days, compared to about 46 days for the other case.

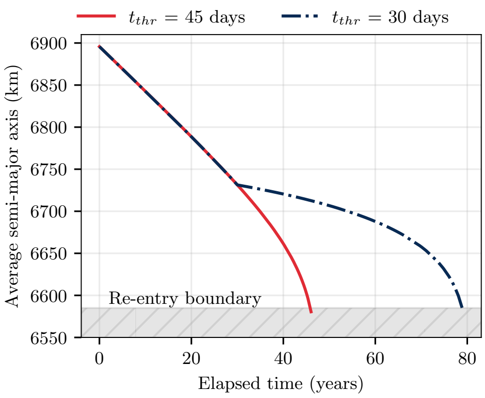

Figure 8: Average semi-major axis over time for different firing durations (t_{thr}).

Thus, by varying t_{thr} a Pareto optimal front containing classical optimization objectives can be obtained, as shown in Figure 9. Each point of the Pareto optimal front represents a feasible solution, with a different decay profile. The trade-off between time and propulsive effort is evident.

This result is generated considering the mean magnitude, nominal scenario Schatten prediction [20] and considering the FEEP thruster from Table 3.

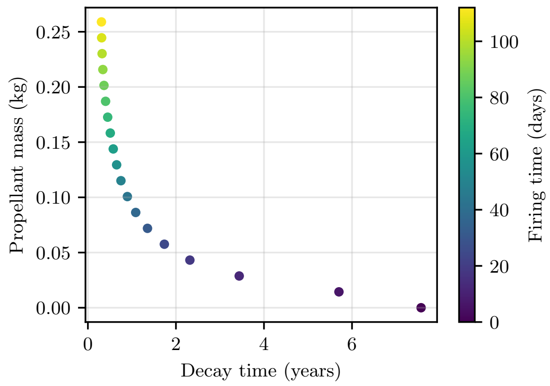

Figure 9: Propellant mass versus decay time, with firing time as a parameter.

By applying the methodology presented in Section 3, it is possible to obtain the collision probability for each point. A new Pareto front can be explored: for example, Figure 10 displays collision probability versus propellant mass.

It appears that larger propulsive effort (higher ΔV, m_p and t_{thr}), translates into a reduction of collision probability and risk. It is possible to see that this is related to the reduction in decay time. Although this latter link is easily identifiable via Eq. (8), this methodology allows computing the probability and designing the deorbiting maneuver based on the acceptable collision probability.

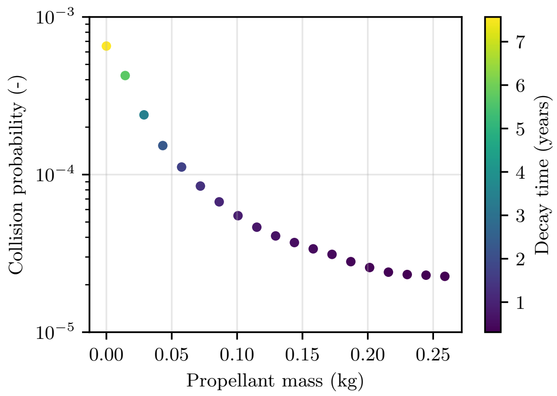

Figure 10: Decay time versus propellant mass, with firing time as a parameter.

4.3. Atmospheric drag uncertainty analysis

A study on the impact of atmospheric drag uncertainty on the decay predictions has been carried out, applying the methodology outlined in the previous subsection. Specifically, the Schatten atmospheric density prediction bounds at $\pm 2\sigma$ have been considered to generate maps of probable deorbiting solutions.

Figure 11 extends the analysis from Figure 9, illustrating the spread introduced by the uncertainty considered. Notably, when minimal propulsive effort is applied, the final decay time uncertainty is substantial. Conversely, increasing propulsive effort significantly reduces this uncertainty.

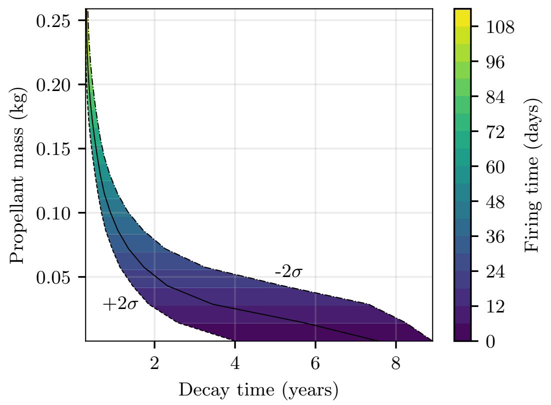

Figure 11: Decay time, propellant mass, and firing time with $\pm 2\sigma$ uncertainty bounds.

Figure 12 expands on Figure 10, depicting the evolution of collision probability throughout the decay trajectory as a function of propellant mass, with decay time represented by the color bar. While increased propellant expenditure inherently reduces collision risk, the associated uncertainty remains mostly unchanged.

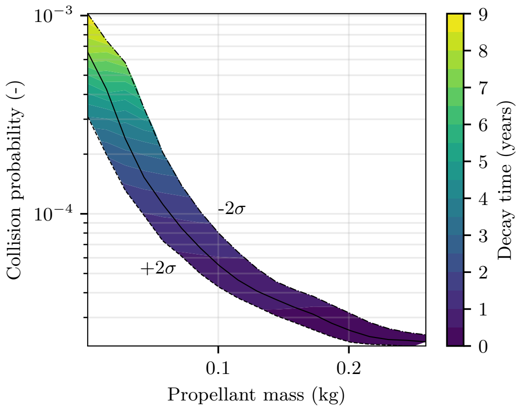

Figure 12: Propellant mass, collision probability, and decay time with $\pm 2\sigma$ uncertainty bounds.

To further investigate these effects, Figure 13 illustrates the correlation between decay time and collision probability. While longer decay times generally correspond to higher collision probabilities, the specific decay trajectory (considering all orbital elements evolution) introduces slight variations in the collision risk estimation.

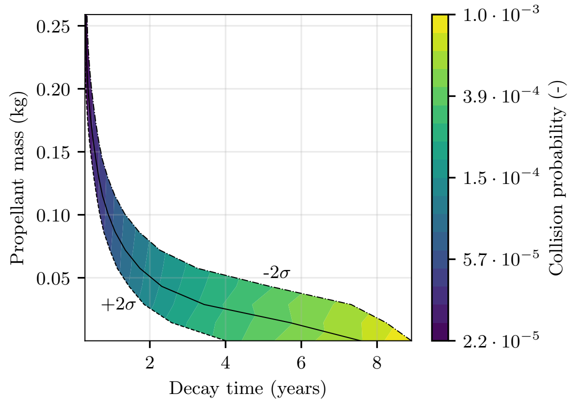

Figure 13: Propellant mass, decay time, and collision probability with $\pm 2\sigma$ uncertainty bounds.

Finally, Figure 14 highlights the relationship between collision probability and decay time. The red line represents the $n = 1$ case, corresponding to a single ARES run on the initial orbit. Notably, this curve falls outside the computed uncertainty bounds, demonstrating that the methodology presented provides improvements beyond the intrinsic uncertainty of the process.

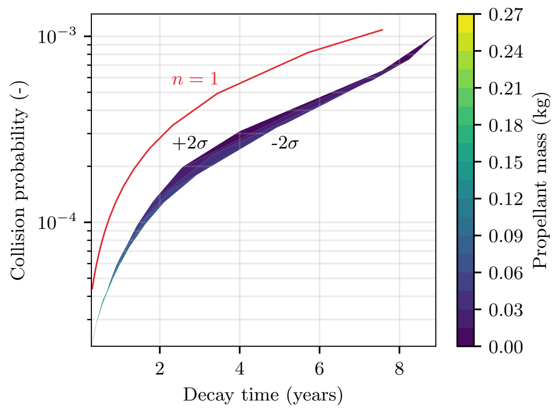

Figure 14: Decay time, collision probability, and propellant mass with $\pm 2\sigma$ uncertainty bounds. The result for a single interval ($n = 1$) is also shown.

4.4. Propulsion system analysis

A comparison of three different electric propulsion technologies is presented in this section. The systems analyzed are based on three commercial products, and their performance parameters are summarized in Table 3.

For all systems, the power consumption is compatible with the satellite's solar panel area and expected power generation at end-of-life. This analysis assumes constant solar activity, with $F10.7 = 150$ and $A_p = 16$.

Figure 15 illustrates the Pareto front of propellant mass versus decay time for the three thrusters. As expected, the FEEP system, with its higher specific impulse, requires the least propellant. The HET system could, in theory, enable the shortest decay times, but its maximum available propellant imposes a constraint. Consequently, ATHENA emerges as the fastest solution.

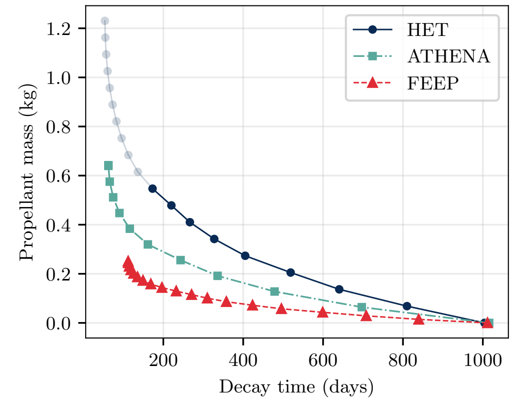

Figure 15: Propellant mass versus decay time for propulsion systems considered.

Figure 16 presents the probability of collision throughout the deorbiting trajectory as a function of firing time for all the systems considered. The results indicate that the FEEP system can reduce the collision probability to approximately 1.4×10^{-5} with a firing duration of about 112 days. The HET system achieves similar values, constrained by the propellant mass limitation (maximum m_p as indicated in the Figure). In a hypothetical scenario with a larger propellant tank, the collision probability could be further reduced to approximately 6×10^{-6}. Finally, the ATHENA system can lower the collision probability to around 7×10^{-6} with a maneuver duration of 68.5 days.

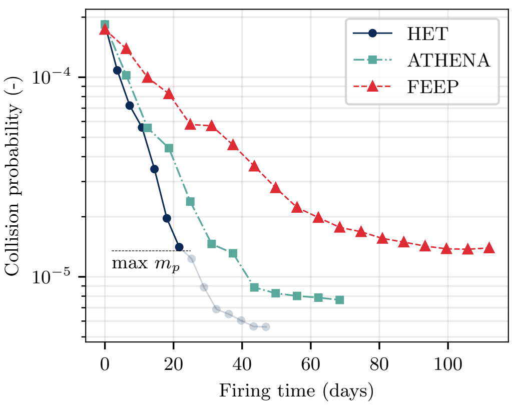

Figure 16: Probability of collision versus firing time for the systems considered.

5. CONCLUSIONS

This paper presents a multi-objective methodology for optimizing deorbiting maneuvers, minimizing both propulsive effort and collision probability. It integrates orbital dynamics—accounting for Earth's oblateness and atmospheric drag—with a DRAMA's ARES extension to compute collision probability throughout the decay trajectory via discretization.

An optimizer selects the firing time, followed by numerical propagation and discretization. Collision probability is computed for each interval using ARES, capturing evolving orbital conditions. This iterative process yields optimal solutions for propellant mass, decay time, and collision probability, enabling a more accurate risk assessment of deorbiting satellites.

Analysis of discretization intervals shows that at least 40 intervals balance computational cost and accuracy, keeping the error below 5%. Time-based discretization also ensures better stability and convergence than a semi-major axis-based approach.

The study further examines atmospheric drag uncertainty and propulsion system selection, revealing key findings:

1. The proposed methodology significantly improves accuracy of the collision probability estimation throughout the decay trajectory.
2. Higher ΔV/propellant mass reduces collision probability, mainly due to shorter decay time.
3. With model uncertainties (e.g., atmospheric density), low propulsion effort leads to significant decay time variability, while higher effort improves predictability.
4. The methodology enables rapid propulsion trade-offs: among the systems analyzed, FEEP is the most propellant-efficient, while the electrospray achieves the fastest decay.
5. This approach has broader implications, including potential applications in policy-making and integration with future space traffic management frameworks, as it allows more precise estimation of collision probability during the decommissioning phase.

In conclusion, this paper presents a methodology that provides an efficient means to compute collision probability for deorbiting satellites, offering valuable insights for optimizing decay strategies. The findings contribute to space debris mitigation and inform mission planning.

Future work may focus on the study of more complex guidance laws and the analysis of a broader range of deorbiting technologies, such as chemical propulsion, tethers, or drag augmentation systems.

REFERENCES

1. (2021). MP42 datasheet. Accessed: 2024-02-09, https://nanoavionics.com/small-satellite-buses/microsatellite-bus-mp42/.

2. Chen, Y. et al. (2020). Optimal mission planning of active space debris removal based on genetic algorithm. *IOP Conference Series: Materials Science and Engineering*, 715:012025. doi: https://iopscience.iop.org/article/10.1088/1757-899X/715/1/012025/pdf.

3. Colombo, C., Rossi, A., Dalla Vedova, F., Braun, V., Bastida Virgili, B., and Krag, H. (2017). Drag and solar sail deorbiting: Re-entry time versus cumulative collision probability. https://re.public.polimi.it/retrieve/e0c31c0c-9c62-4599-e053-1705fe0aef77/COLOC04-17.pdf.

4. Di Pasquale, G., Sanjurjo-Rivo, M., and Pérez Grande, D. (2024). A multi-objective variable-specific impulse maneuvers optimization methodology. *Advances in Space Research*, 73(1):20–30. doi: https://www.sciencedirect.com/science/article/pii/S0273117723008372.

5. Diserens, S., Lewis, H. G., and Fliege, J. (2020). Assessing collision algorithms for the newspace era. *Journal of Space Safety Engineering*, 7(3):274–281. doi: https://www.sciencedirect.com/science/article/abs/pii/S2468896720300859.

6. Edelbaum, T. N. (1961). Propulsion Requirements for Controllable Satellites. *ARS Journal*, 31(8):1079–1089. Publisher: American Institute of Aeronautics and Astronautics.

7. ENPULSION (2025). Enpulsion nano. Accessed: 04-Mar-2025.

8. European Space Agency (2013). ESA's MASTER Software Tool. https://www.esa.int/ESA_Multimedia/Images/2013/04/ESA_s_MASTER_software_tool. Accessed: 2024-09-25.

9. European Space Agency (2024a). Ares module documentation - drama python package. https://sdup.esoc.esa.int/drama/python_package_docs/modules/ares.html. Accessed: 2024-09-25.

10. European Space Agency (2024b). Space debris user portal (sdup). https://sdup.esoc.esa.int/. Accessed: 2024-09-25.

11. European Space Agency (ESA) (2024). Esa's zero debris approach. https://www.esa.int/Space_Safety/Clean_Space/ESA_s_Zero_Debris_approach. Accessed: 2024-09-17.

12. Exotrail (2024). Spaceware - exotrail. Accessed: 2024-02-09, https://www.exotrail.com/product/spaceware.

13. Fukii, S., Sakai, D., Yoshimura, Y., Matsushita, Y., Hanada, T., Itaya, Y., and Fukushima, T. (2022). Assessing collision probability in low-thrust deorbit. *Journal of Space Safety Engineering*, 9(1):47–55. doi: https://doi.org/10.1016/j.jsse.2021.11.002.

14. Gaglio, E. and Bevilacqua, R. (2023). Time optimal drag-based targeted de-orbiting for low earth orbit. *Acta Astronautica*, 207:316–330. doi: https://doi.org/10.1016/j.actaastro.2023.03.011.

15. Gelhaus, J., Sánchez-Ortiz, N., Braun, V., Kebschull, C., de Oliveira, J. C., Domínguez-González, R., Wiedemann, C., Krag, H., and Vörsmann, P. (2013). Upgrade of drama: Esa's space debris mitigation analysis tool suite. In *Proceedings of the 6^{th} European Conference on Space Debris*, Darmstadt, Germany. ESA SP-723, April 22–25, 2013.

16. Krier, G. (2017). Satellite Collision Probability for Long-Term Encounters and Arbitrary Primary Satellite Shape. In *Proceedings of the 7^{th} European Conference on Space Debris*.

17. Picone, J. M., Hedin, A. E., Drob, D. P., and Aikin, A. C. (2002). NRLMSISE-00 empirical model of the atmosphere: Statistical comparisons and scientific issues. *Journal of Geophysical Research: Space Physics*, 107(A12):SIA 15–1–SIA 15–16. doi: https://onlinelibrary.wiley.com/doi/abs/10.1029/2002JA009430.

18. Radtke, J., Kebschull, C., and Stoll, E. (2017a). Interactions of the space debris environment with mega constellations—using the example of the oneweb constellation. *Acta Astronautica*, 131:55–68. doi: 10.1016/j.actaastro.2016.11.021.

19. Radtke, J., Mueller, S., Schaus, V., and Stoll, E. (2017b). Luca2 - an enhanced long-term utility for collision analysis. In *Proceedings of the 7^{th} European Conference on Space Debris*, Darmstadt, Germany. ESA Space Debris Office.

20. Schatten, K. (2002). Solar activity prediction: Timing predictors and cycle 24. *Journal of Geophysical Research: Space Physics*, 107(A11):SSH 15–7. doi: 10.1029/2002JA009404.

21. Steyn, W. (2024). De-orbiting strategies. https://s3vi.ndc.nasa.gov/ssri-kb/static/resources/DeOrbit_whs.pdf. Accessed: 2024-01-01.

22. Verri, A. (2021). Low-thrust many-revolutions maneuver optimization for future active debris removal application. https://webthesis.biblio.polito.it/18293/1/tesi.pdf.

23. Villegas, D., Correyero, S., Wijnen, M., and Fajardo, P. (2022). Indirect Characterization of ATHENA Performance, a Novel Externally Wetted Electrospray Propulsion System. In *Space Propulsion Conference 2022*.

24. Vokrouhlický, D., Pokorný, P., and Nesvorný, D. (2012). Öpik-type collision probability for high-inclination orbits. *Icarus*, 219:150–160.

25. Walker, M. J. H., Ireland, B., and Owens, J. (1985). A set modified equinoctial orbit elements. *Celestial mechanics*, 36(4):409–419.

26. Öpik, E. J. (1951). Collision probabilities with the planets and the distribution of interplanetary matter. *Proceedings of the Royal Irish Academy, Section A*, 54:165–199. doi: https://www.jstor.org/stable/20488472.